Featured in Physics

Frequency Comb from a Single Driven Nonlinear Nanomechanical Mode

J. S. Ochs,[1,*] D. K. J. Boneß,[1] G. Rastelli,[2] M. Seitner,[1] W. Belzig,[1] M. I. Dykman,[3,†] and E. M. Weig[1,4,5,6,‡]

[1]*Department of Physics, University of Konstanz, 78457 Konstanz, Germany*
[2]*Pitaevskii Center on Bose-Einstein Condensation, CNR-INO and Dipartimento di Fisica dell'Università di Trento, Via Sommarive 14, 38123 Trento, Italy*
[3]*Department of Physics and Astronomy, Michigan State University, East Lansing, Michigan 48824, USA*
[4]*Department of Electrical Engineering, School of Computation, Information and Technology, Technical University of Munich, 85748 Garching, Germany*
[5]*Munich Center for Quantum Science and Technology (MCQST), 80799 Munich, Germany*
[6]*TUM Center for Quantum Engineering (ZQE), 85748 Garching, Germany*

(Received 26 July 2022; accepted 14 October 2022; published 18 November 2022)

Phononic frequency combs have attracted increasing attention both as a qualitatively new type of nonlinear phenomena in vibrational systems and from the point of view of applications. It is commonly believed that at least two modes must be involved in generating a comb. We demonstrate that a comb can be generated by a single nanomechanical mode driven by a resonant monochromatic drive. The comb emerges where the drive is still weak, so the anharmonic part of the mode potential energy remains small. We relate the experimental observation to a negative nonlinear friction induced by the resonant drive, which makes the vibrations at the drive frequency unstable. We directly map the measured trajectories of the emerging oscillations in the rotating frame and show how these oscillations lead to the frequency comb in the laboratory frame. The results go beyond nanomechanics and suggest a qualitatively new approach to generating tunable frequency combs in single-mode vibrational systems. They demonstrate new sides of the interplay of conservative and dissipative nonlinearities in driven systems.

DOI: 10.1103/PhysRevX.12.041019

Subject Areas: Condensed Matter Physics
Nanophysics, Nonlinear Dynamics

I. INTRODUCTION

Since their discovery at the turn of the 21st century [1,2], frequency combs have revolutionized the field of metrology, from unprecedentedly accurate timekeeping to molecule sensing, to distance measurements [3–5]. Frequency combs consist of a series of narrow spectral lines [1,2]. Of central importance for metrology is that the lines are equally spaced. This feature is a consequence of the strong nonlinearity of the radiation sources. In lasers, such nonlinearity can lead to mode locking, which, in turn, leads to generation of frequency combs. It also underlies the electro-optic comb generation. In laser-driven microresonators, broadband optical combs with extremely narrow peaks emerge as a result of four-wave mixing induced by the Kerr nonlinearity [6,7]. A frequency comb associated with a strongly nonlinear parametric excitation has been seen in a superconducting microwave cavity [8].

Frequency combs have also been observed in nanomechanical vibrational systems [9–22]. Such combs are often called phononic. They cover a broad frequency range and have the advantage of being tunable *in situ*. They have been observed by nonlinearly mixing two drive frequencies, or by using nonlinear resonance or strong linear coupling between different vibrational modes. For a single-frequency drive, at least two modes were involved, somewhat reminiscent of the multimode frequency combs of laser radiation.

The analysis of the frequency combs has led to a general conclusion [19,23,24] that it is necessary to have at least two coupled modes, with at least one of them driven, to generate a comb. This conclusion can be understood by noting that coupled modes can resonantly exchange energy with each other, an observation that, for nonlinear coupling, goes back to Laplace and Poincarè on the classical side and to the Fermi resonance on the quantum side [25,26]. The ensuing oscillations are sustained by the external periodic drive. They are slow compared to the mode frequencies and the drive frequency, but they can be strongly nonsinusoidal;

*Formerly Huber.
†dykmanm@msu.edu
‡eva.weig@tum.de

thus, their spectrum consists of multiple equidistant lines separated by their frequency. When superposed on the forced vibrations at the drive frequency, this spectrum transforms into a frequency comb.

In this paper, we demonstrate that the onset of a frequency comb in a vibrational system does not require mode-mode coupling. We observe a comb using a nanomechanical resonator driven by a single-frequency resonant drive in the regime where only one mode is involved in the dynamics. The occurrence of the comb results primarily from the combination of two factors. First, resonant driving can open a relaxation channel that leads to a negative friction force [27]. It makes the state of stationary forced vibrations at the drive frequency unstable. As a result, the mode starts precessing about this state. In the frame that rotates at the drive frequency, the precession looks like vibrations. The second factor is that these vibrations are strongly nonsinusoidal, which leads to a frequency comb, as in the case of coupled modes. As we show, the number of pronounced spectral lines in the comb and the spacing between them can be controlled just by varying the amplitude and frequency of the drive.

The observation of the comb has been facilitated by our nanomechanical vibrational mode being weakly damped. Because the damping is weak, even a comparatively weak driving-induced negative friction force can overcome it, leading to an instability of the stationary forced vibrations. For the same reason, the nonlinearity of the mode comes into play already for a comparatively weak driving provided the driving is resonant. A feature of the nonlinearity is that, in a sense, it is weak: The nonlinear part of the vibration energy is much smaller than the harmonic part. However, as viewed in the rotating frame, where the harmonic part is largely compensated, the nonlinearity can be strong because it is competing with the weak damping. It is the strong nonlinearity in the rotating frame that makes the vibrations in this frame strongly nonsinusoidal, leading to multiple lines in the comb spectrum.

The occurrence of a negative friction force in vibrational systems is well known for nonresonant driving [28]; it plays an important role in cavity optomechanics [29]. However, negative friction may also emerge [27] for resonant driving [30], as also suggested by experiment [31]. The resonantly induced friction force (RIFF) is nonlinear in the mode coordinate. Therefore, it only comes into play once the vibration amplitude becomes sufficiently large. We observe its effect only on the large-amplitude branch of the response curve.

II. SETUP AND CHARACTERIZATION

The investigated nanomechanical resonator is a freely suspended string resonator, similar to the one depicted in Fig. 1(a). It is fabricated from prestressed silicon nitride on a fused silica substrate, facilitating ultrahigh-quality factors greater than or around 10^5 at room temperature. The string has a length of 55 μm, a width of 270 nm, and a thickness

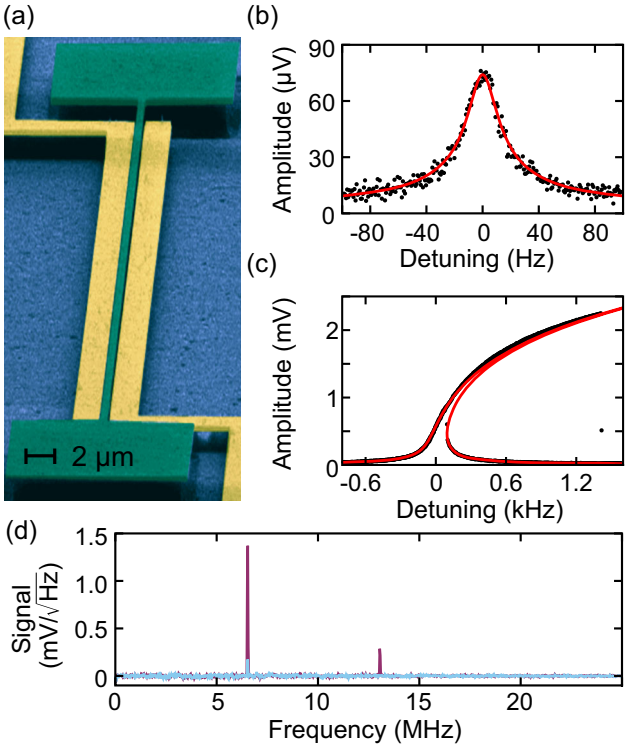

FIG. 1. Nanomechanical string resonator in the single-mode regime. (a) Scanning electron micrograph of the doubly clamped silicon nitride string resonator (green) and two control electrodes (yellow). (b) Linear response for a drive power of −56 dBm along with a Lorentzian fit (solid red line). A constant noise background has been subtracted from the data (1.5×10^{-6} V). (c) Amplitude of forced vibrations for a moderately strong drive power of −24 dBm as a function of drive frequency along with a fit (solid red line, see Appendix B). (d) Vibration spectra for a resonant drive applied at the OOP mode in the linear regime (−46 dBm, light blue), and for a stronger drive (5 dBm, purple) that exhibits an overtone at twice the drive frequency. Even under strong driving, no other modes are excited. A noise background has been subtracted from the data.

of 100 nm. Integrated dielectric transduction combined with microwave cavity-enhanced heterodyne detection, described in Refs. [32–34], is implemented via the two gold electrodes [also apparent in Fig. 1(a)] and allows one to actuate and detect the motion of the resonator. All measurements are performed at a constant dc voltage of 5 V, under vacuum at a pressure below 10^{-4} mbar and at room temperature of 293 K. The vibration amplitude is proportional to the output signal, which is measured in volts, in the experimental setting. Therefore, in all experimental data, the displacement amplitude of the nanoresonator is given in volts (see also Appendix B).

The fundamental flexural out-of-plane (OOP) mode of the resonator is characterized in the linear as well as in the nonlinear regime by driving the mode with a single-tone drive $F\cos(2\pi f_d t)$ applied on or near resonance. From the linear response measurement (black dots) and a Lorentzian

fit (solid red line), shown in Fig. 1(b), one obtains the mode eigenfrequency $f_0 = \omega_0/2\pi \approx 6.528$ MHz, the linewidth $2\Gamma/2\pi \approx 21$ Hz, and, with that, the Q factor of $Q \approx 310\,000$.

The nonlinear response of the resonator as a function of the detuning $f_d - f_0$ is shown in Fig. 1(c). In the presented parameter range, the forced vibrations are nearly sinusoidal. The stationary value of the mode coordinate is $q(t) \approx A\cos(2\pi f_d t + \phi)$, where A and ϕ are the vibration amplitude and phase.

In nanomechanics, resonant nonlinear response is most frequently described by the Duffing (sometimes also called Kerr) model, in which the nonlinear part of the potential of the mode $U(q)$ has the form $M\gamma q^4/4$ [35], where M is the effective mass of the mode and γ is the Duffing parameter. The response in Fig. 1(c) cannot be fit to the standard Duffing curve. The deviation is due to the resonator lacking inversion symmetry, for example, due to the term proportional to q^3 in $U(q)$ [36]. For the studied mode, it leads to a significant reduction of the positive "bare" value of γ, i.e., $\gamma \to \gamma_{\rm eff}$, in the regime of comparatively small vibration amplitudes [37].

In the experiment, the mode amplitude and the amplitude of the driving force are measured in volts. In these units, the renormalized value of the Duffing parameter at comparatively small vibration amplitudes below 1 mV is $\gamma_{\rm eff}^{(\rm V)}/(2\pi)^2 \approx 2.57 \times 10^{15}\ {\rm V}^{-2}\,{\rm s}^{-2}$. The full theoretical analysis, including the full response curve in Fig. 1(c), is given in Sec. IV (see also Appendix A).

The dc voltage is chosen in such a way as to operate the system in the single-mode regime. No other modes are excited where the OOP mode is driven on or close to resonance. Figure 1(d) displays the vibration spectrum for a drive applied at the eigenfrequency of the OOP mode. In the linear response regime, only forced vibrations at the drive frequency are observed (light blue line). For a stronger drive, we observe an overtone at twice the drive frequency (purple line), as expected for a resonator with broken inversion symmetry. We do not see signals at other frequencies. The full mode spectrum of the device is discussed in Appendix C.

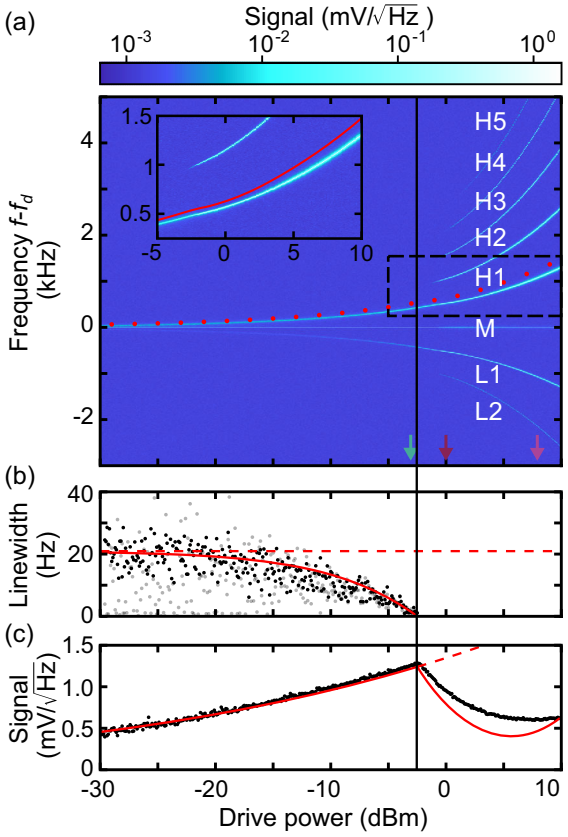

FIG. 2. Frequency comb induced by resonant drive. (a) Power spectra of the mode measured for increasing drive power at $f_d = f_0$. The transition from the regime of two thermal-noise-induced satellite peaks to the frequency comb consisting of a series of equidistantly spaced, multiple satellite peaks is clearly seen. It occurs at $\mathcal{P}_{\rm th} = -2.5$ dBm (black vertical line). The red dots show the theoretical model for H_1. The inset shows the magnified region inside the dashed box. Arrows indicate drive power of the line cuts depicted in Fig. 3(a). (b) Extracted linewidth of the two thermal noise-induced satellite peaks H_1 (black) and L_1 (gray) as a function of the drive power. The dashed line represents the prediction based on the theory that disregards driving-induced friction, whereas the solid line includes it [see Eqs. (4) and (5)]. (c) Amplitude of forced vibrations at $f_d = f_0$ as a function of the drive power. The dashed line represents the prediction based on the theory that disregards driving-induced friction, whereas the solid line includes it [see Eqs. (4) and (5)].

III. EXPERIMENTAL OBSERVATIONS

A. Driving on resonance

In Fig. 2(a), we show the power spectra of the OOP mode driven on resonance, $f_d = f_0$, for the drive power in the range from −30 dBm to +10 dBm. For drive powers below −15 dBm, besides the main-tone (M) peak at the drive frequency f_d, we observe two thermal-noise-induced satellite peaks, which appear in the spectrum symmetrically to the left (L_1) and right (H_1) of M. The onset of such satellites was theoretically predicted (see Ref. [38] and references therein). The satellites, as well as the spectral evidence of squeezing encoded in their unequal brightness, are discussed in Ref. [39].

As the drive power approaches the threshold value $\mathcal{P}_{\rm th} \approx -2.5$ dBm (black vertical line), the noise-induced satellites (H_1, L_1) evolve into much narrower peaks. For increasing power, we resolve additional, equally spaced, satellite peaks forming a frequency comb. We label them as (H_2, L_2), (H_3, L_3), etc., with H referring to the higher-frequency and L to the lower-frequency satellites. Note that the lower-frequency satellites are less intense than the higher-frequency ones.

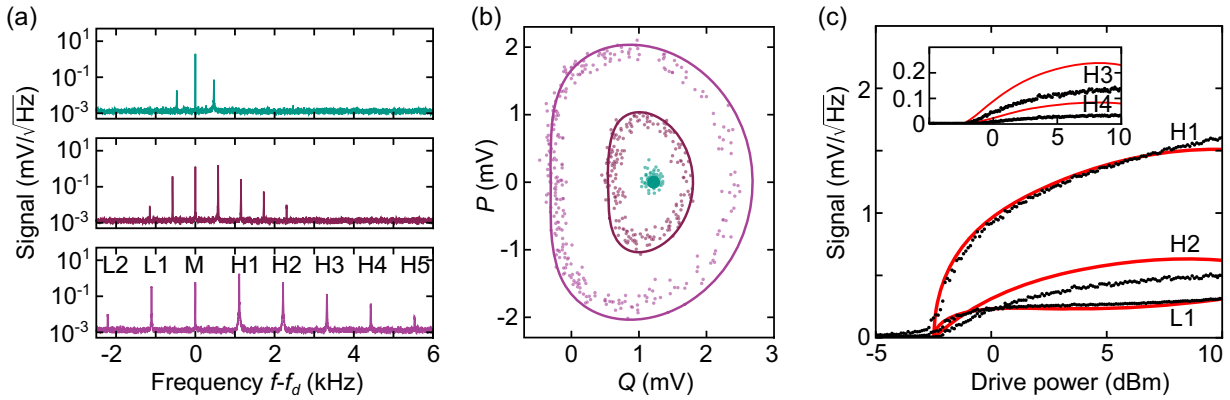

FIG. 3. Spectral vs homodyne measurement. (a) Frequency combs at drive power −3 dBm (top), −1 dBm (center), and 8 dBm (bottom). Data are taken from line cuts of Fig. 2(a) indicated by small arrows. (b) Trajectories in the rotating frame for the same drive powers as in (a). Data have been rescaled as described in Appendix B. Solid lines depict the theoretical model. (c) Amplitude of the satellites L_1, H_1, H_2 as well as H_3 and H_4 (magnified in the inset) from Fig. 2(a) (black dots), compared to the Fourier components obtained from the theoretical model (red lines).

The linewidths of the first higher- and lower-frequency peaks H_1 and L_1 are explored in more detail in Fig. 2(b). The linewidth is found from a Lorentzian fit. It remains at a constant value of approximately 21 Hz up to a drive power of −15 dBm. This value corresponds to the linear damping rate of the OOP mode. For larger drive powers, the linewidth gradually decreases until at $\mathcal{P}_{\mathrm{th}}$ it reaches the resolution limit 1 Hz of our measurement device. Respectively, in Fig. 2(b), we do not show the linewidth for $\mathcal{P} > \mathcal{P}_{\mathrm{th}}$. The linewidths of higher-order satellites, which appear for $\mathcal{P} > \mathcal{P}_{\mathrm{th}}$, could not be resolved either.

Figure 2(c) extracts the amplitude of the main tone, i.e., the amplitude of the forced vibrations at $f_d = f_0$, as a function of the drive power. The signal increases with the drive power until $\mathcal{P}_{\mathrm{th}}$. At the threshold power, the amplitude of the forced vibrations exhibits a kink and abruptly starts to decrease.

Strikingly, the succinct features of Figs. 2(b) and 2(c)—the linewidth reaching the resolution limit and the kink in the amplitude of the forced vibrations—coincide with the emergence of the frequency comb at $\mathcal{P}_{\mathrm{th}}$ (black vertical line).

Figure 3(a) presents line cuts of Fig. 2(a) at the drive powers indicated in Fig. 2(a) by small arrows. Beyond $\mathcal{P}_{\mathrm{th}}$, the intensity of the satellite peaks forming the frequency comb strongly increases with the increasing drive strength. It is noteworthy to observe that some satellites even exceed the intensity of the main tone.

In addition to the spectral measurements discussed so far, we directly record the trajectories of the system in the rotating frame using a homodyne measurement. A fast lock-in amplifier is employed to sample both the in-phase and quadrature signals of the driven resonator over time. In order to capture the frequency comb, the measurement is performed with a large bandwidth of 10 kHz. Figure 3(b) plots the obtained trajectories in the space of the in-phase (Q) and quadrature (P) components, i.e., in the phase space of the rotating frame. For a drive power of −3 dBm, corresponding to the top panel in Fig. 3(a), the system is still in a stable state of forced vibrations, such that the trajectory mostly stays within a thermal-noise-broadened ellipse centered at the value of Q and P in the stable state. For a larger drive power of −1 dBm, beyond the instability threshold, the system is clearly on a limit cycle. It represents the self-sustained oscillations of the resonator in the rotating frame. The shape of the trajectory is profoundly nonelliptical, which means that the vibrations of $Q(t)$ and $P(t)$ are nonsinusoidal. This is consistent with the observation of multiple satellites in the power spectrum in the middle panel of Fig. 3(a). For a still-larger drive power of 8 dBm, a larger and even more nonelliptical limit cycle is observed, which is in line with the bottom panel of Fig. 3(a).

Interestingly, the trajectories are practically symmetric with respect to the axis $P = 0$. As we explain in Sec. IV, this is a consequence of a very small decay rate of the mode. The amplitude of the first lower and the first four higher satellites—L_1, and H_1 to H_4—is plotted in Fig. 3(c) as a function of drive power.

B. Frequency comb as a function of the drive detuning

Along with the onset of the frequency comb with the increasing drive amplitude, we have studied the emergence of a comb with the varying drive frequency $f_d - f_0$. The results for a fixed drive power of 0 dBm are shown in Figs. 4 and 5. For this drive power, and at finite detuning $f_d - f_0 > 0$, the spectra display an even more elaborate frequency comb than in Fig. 3.

For each measurement, the resonator is initialized in the large-amplitude state by sweeping up the drive frequency from 30 kHz below f_0 to the desired drive frequency f_d prior to recording the power spectrum. For a large negative

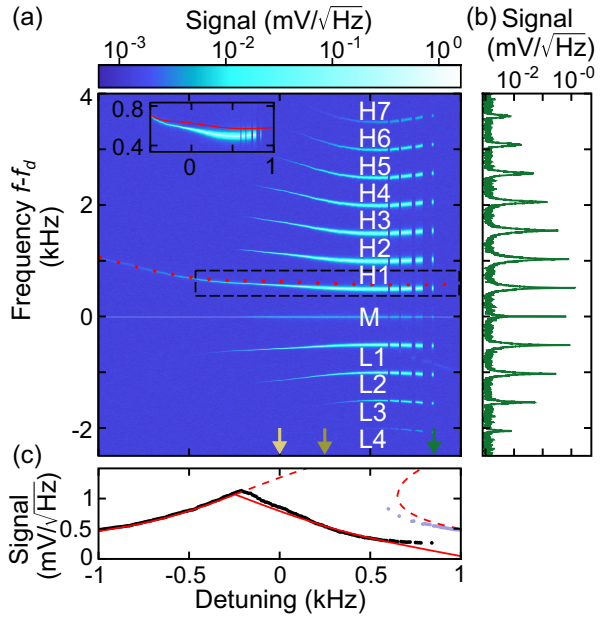

FIG. 4. Frequency comb for detuned drive. (a) Power spectra measured for increasing detuning $f_d - f_0$ at a fixed drive power of 0 dBm. The dotted line represents the theoretical model for H_1. The inset magnifies the region indicated by the dashed box. Arrows indicate drive power of the trajectories depicted in Fig. 5(a). (b) Frequency comb in line cut of diagram (a) taken at a detuning of 840 Hz (dark green arrow). (c) Amplitude of forced vibrations at f_d as a function of detuning extracted from diagram (a). Black data points refer to the large-amplitude solution, whereas light purple indicates the small-amplitude solution for which there is no instability. The dashed line represents the prediction based on the theory that disregards driving-induced friction, whereas the solid line includes it; see Eqs. (4) and (5).

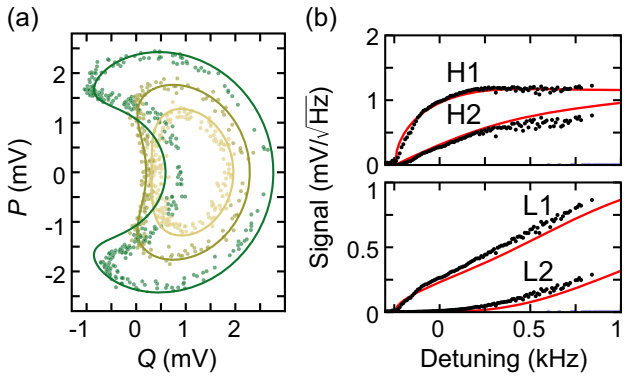

FIG. 5. Nonsinusoidal trajectories for detuned drive. (a) Trajectories in the rotating frame for a detuning of 0 Hz (yellow), 250 Hz (olive), and 850 Hz (dark green) at a drive power of 0 dBm. Data have been rescaled as described in Appendix B. (b) Amplitude of the satellites H_1, H_2 (top) as well as L_1, L_2 (bottom) as a function of detuning from Fig. 4(a) (black dots), compared to the Fourier components obtained from the theory (red lines).

detuning, the system remains stable for the selected drive power. The instability occurs at a detuning of −210 Hz, and for increasing detuning, an increasingly multiple-line frequency comb rapidly evolves. The number of visible lines is significantly larger than for the case of a resonant drive, as also apparent from the line cut in Fig. 4(b).

The comb only exists in the detuning range limited by the bifurcational value at which the large-amplitude branch of the response curve disappears as a whole, cf. Fig. 1(c). On the small-amplitude branch, the mode does not display a frequency comb. The rate of switching to the small-amplitude branch increases exponentially as the system approaches the bifurcation point [35], and so does the probability of switching during the measurement. The randomness of the switching is manifested in the apparent gaps in the comb and in the jumps in the vibration amplitude of Figs. 4(a) and 4(c), respectively. Both signatures result from such switching. The power spectra have been obtained with a 10-Hz increment. Therefore, for example, the two gaps and the respective jumps at 600 Hz and 660 Hz correspond to single random switching events. Counterintuitively, the amplitude of the vibrations at the drive frequency sharply increases when the system switches to the small-amplitude branch, as apparent from Fig. 4(c). The forced vibrations at the drive frequency remain stable on this branch; there is no frequency comb.

Figure 5(a) depicts three trajectories measured for a detuned drive [color-coded detuning marked by arrows in Fig. 4(a)], all at the same drive power. For increasing detuning, the size and asymmetry of the observed limit cycles clearly increase, giving rise to a horseshoe-like trajectory. The presented trajectories are significantly more asymmetric than those for a resonant drive, in agreement with the higher number of frequency comb lines observed. The amplitude of the first two lower and higher satellite peaks is extracted as a function of the detuning in Fig. 5(b).

IV. INTERPRETATION

A remarkable feature of the studied nanomechanical mode is that it is weakly damped not only in the laboratory frame, $\Gamma \ll \omega_0 = 2\pi f_0$, but also in the rotating frame. To understand the experimental observations, it first is necessary to understand the dynamics of the mode in the absence of dissipation. Understanding the dissipation mechanisms is the next step.

A. Hamiltonian dynamics of the driven mode

We start with the Hamiltonian dynamics in the laboratory frame and then proceed to the Hamiltonian dynamics in the rotating frame. In the studied regime, the anharmonic part of the potential energy of the mode $U(q)$ is small compared to the harmonic part $(p^2/2M) + (M\omega_0^2 q^2/2)$, where p is the momentum in the laboratory frame. The major effect of the mode nonlinearity is the dependence of

the vibration frequency on the mode energy E or, equivalently, on the action variable I, with the frequency being $\omega(I) = dE/dI$ [36]. In the Duffing model, $\omega(I) \approx \omega_0 + \alpha_1 I$ for small I, with $\alpha_1 = 3\gamma/4M\omega_0^2$ [$\omega_0 \equiv \omega(0)$]. More generally, α_1 is proportional to the effective Duffing parameter γ_{eff} rather than γ. Thus, α_1 is directly accessible from the experiment in the regime of comparatively small vibration amplitudes even if the Duffing model does not hold for increasing amplitudes.

The peculiarity of the studied mode is the significant reduction of γ_{eff} compared to γ, which means that α_1 is small. Therefore, to describe the response for larger amplitudes, it is necessary to keep a higher-order term in the expansion of the frequency in I, i.e., to set $\omega(I) \approx \omega_0 + \alpha_1 I + \alpha_2 I^2$. This corresponds to the Hamiltonian of the mode in the laboratory frame of the form

$$H_0 = \omega_0 I + \frac{1}{2}\alpha_1 I^2 + \frac{1}{3}\alpha_2 I^3. \tag{1}$$

This form is general. It incorporates not only the nonlinearity of the isolated mode but also the renormalization of the mode parameters due to a nonresonant coupling to other modes of the nanoresonator, including phonons [35]. The parameter α_2 has contributions quadratic in γ and also contributions from the terms $\propto q^3$, q^5, q^6 in the potential $U(q)$; see Appendix A 1. However, all these terms are renormalized. The parameters α_1 and α_2 are the only relevant parameters of the conservative dynamics in the whole range of moderately large vibration amplitudes.

The effect of the resonant driving force is described by incorporating into the mode Hamiltonian the term $H_F = -qF\cos\omega_d t$ ($\omega_d = 2\pi f_d$). This effect becomes strong already for a comparatively weak force amplitude F, as F is "competing" with the small frequency detuning $|\omega_d - \omega_0| \ll \omega_d$. The mode dynamics can be analyzed using the conventional method of averaging [25], which, in this case, is the averaging over the drive period $2\pi/\omega_d$. A significant simplification comes from the fact that, in the considered amplitude range, the mode coordinate in H_F can be approximated as $q \approx (2I/M\omega_d)^{1/2}\cos\theta$, where θ is the vibration phase.

The averaged Hamiltonian describes the dynamics of the driven mode in the rotating frame. The mode coordinate Q and momentum P in this frame correspond to the in-phase and quadrature components of the vibrations,

$$Q + iP = [q + i(p/M\omega_d)]\exp(i\omega_d t). \tag{2}$$

In these variables, the Hamiltonian of the driven mode $g(Q,P)$ reads (see Appendix A 1)

$$g(Q,P) = (M\omega_d)^{-1}(H_0 - \omega_d I - QF/2),$$
$$I = M\omega_d(Q^2 + P^2)/2. \tag{3}$$

The dynamical variables Q, P satisfy the standard Hamiltonian equations $\dot{Q} = \partial_P g, \dot{P} = -\partial_Q g$. In quantum terms, the value of g on a Hamiltonian trajectory is the quasienergy of the driven mode [40–43]. Also, the employed method of averaging goes beyond the conventional rotating-wave approximation.

We emphasize that, even though the dynamics in the laboratory frame is weakly nonlinear, the dynamics in the rotating frame is strongly nonlinear. The vibrations $Q(t)$ and $P(t)$ with a given g can be strongly nonsinusoidal. The typical frequencies of these vibrations $\nu(g)$ turn out to be much higher than the decay rate of the mode; that is, the mode is underdamped not only in the laboratory frame but also in the rotating frame. It is this property that determines the shape of the measured trajectories in Figs. 3(b) and 5(a), which are essentially the Hamiltonian trajectories $g(Q,P) =$ const. This means that the measured trajectories directly depict constant-quasienergy contours. Because $g(Q,P) = g(Q,-P)$, the Hamiltonian trajectories are symmetric with respect to the axis $P = 0$. The symmetry of the measured trajectories is a signature of the weak dissipation in the experiment.

For a given $g(Q,P) = g$, the nonsinusoidal trajectories in the rotating frame have multiple, equally spaced, Fourier components separated by $\nu(g)$. As seen from Eq. (2), these components modulate the vibrations of the mode at frequency ω_d in the laboratory frame. Therefore, they are seen in the spectrum of the mode as equidistant lines separated by $\nu(g)$. This underlies the frequency comb observed in the experiment.

B. Instability mechanism

The observation of the instability of forced vibrations with the increasing vibration amplitude and the "soft" onset of the frequency comb suggests that the effective friction force turns to zero at the instability threshold [44]. This implies the existence of a negative nonlinear friction force. Such a force must be increasing with the increasing vibration amplitude so that at the threshold it compensates the conventional friction force $-2M\Gamma\dot{q}$. There are no *a priori* reasons to expect that, if this force is retarded, the retardation time will be so long as to be comparable with the dynamical times in the rotating frame. Therefore, given that we are interested in the dynamics in the rotating frame, in the phenomenological description, retardation can be disregarded.

A simple phenomenological form of the relevant friction force is RIFF [27],

$$F_{\text{RIFF}} = -\eta_{\text{RIFF}} F\cos(\omega_d t)\dot{q}(t)q(t). \tag{4}$$

The force F_{RIFF} has the proper time and spatial symmetry, and the nonlinearity is of the lowest order (quadratic) in the vibration amplitude. A microscopic model of this force was related [27] to the fact that the work by the force averaged

over the period $2\pi/\omega_d$, $[F\cos(\omega_d t)\dot{q}(t)]_{\rm av}$, leads to heating of a nanoresonator. The associated thermal expansion can reduce tension in the nanostructure and thus the mode eigenfrequency. One can easily infer from Fig. 1(c) that the decrease of the eigenfrequency with the increasing vibration amplitude on the upper branch of the response curve can lead to an instability. However, our estimates show that the heating is too weak for the nanoresonator studied in the experiment.

We emphasise that the force $F_{\rm RIFF}$ is small, $|F_{\rm RIFF}| \ll F$. It is beating against the friction force $-2M\Gamma\dot{q}$, whereas in our system, Γ is very small, the smallest parameter with the dimension of frequency. The force $F_{\rm RIFF}$ describes the resonant, dissipative response of the resonator to the lowest order in F. Besides heating, there are other microscopic mechanisms of this force—for example, the displacement-induced retarded modulation of the charge on the resonator, which we believe may be relevant for our system.

We were not able to identify the microscopic mechanism of $F_{\rm RIFF}$ in this system unambiguously. Therefore, we consider $\eta_{\rm RIFF}$ as an adjustable parameter. Replacing $F\cos(\omega_d t)\dot{q}(t) \to [F\cos(\omega_d t)\dot{q}(t)]_{\rm av}$ in Eq. (4) weakly affects the results, and since such a replacement is physically appealing, we use it.

Besides the RIFF, the resonant drive can open another relaxation channel, similar to the driving-induced relaxation for a nonresonant drive in cavity optomechanics [28,29]. It can be understood by thinking that the drive modulates the coupling of the mode to a thermal bath, with the interaction Hamiltonian of the form $H_i = F\cos(\omega_d t)qh_{\rm b}$, where $h_{\rm b}$ depends on the dynamical variables of the bath. The modulation gives rise to the driving-induced decay processes, which change the mode decay rate,

$$\Gamma \to \Gamma + F^2\Gamma_d,$$
$$\Gamma_d = \frac{1}{8\hbar M\omega_0}{\rm Re}\int_0^\infty dt e^{2i\omega_d t}\langle[h_b(t), h_b(0)]\rangle. \quad (5)$$

Here, $\langle\ldots\rangle$ denotes thermal averaging over the states of the bath; see Appendix A 2.

The dependence of $F_{\rm RIFF}$ on the vibration amplitude plays a dual role. On the one hand, the increase of $F_{\rm RIFF}$ with the increasing amplitude leads to the very instability of the stationary state of forced vibrations at $\mathcal{P}_{\rm th}$. On the other hand, once the system starts vibrating in the rotating frame, its mean amplitude in the laboratory frame, which is proportional to $(Q^2+P^2)^{1/2}$, decreases. This is clearly seen in Fig. 2(c). Then, $F_{\rm RIFF}$ decreases with the increasing amplitude of vibrations in the rotating frame. As a result, a stable limit cycle forms in the rotating frame. In the weak-damping limit, it corresponds to vibrations with the value of the quasienergy g such that the dissipative terms including $F_{\rm RIFF}$, averaged over the orbit $g(Q,P) = g$, exactly compensate each other. With the increasing drive power, this g increases, leading to the evolution of the trajectories in Fig. 3(b). We note that vibrations in the rotating frame can also be generated using a feedback loop, as demonstrated by Houri *et al.* [21].

The above nonlinear theory has four parameters: $\alpha_{1,2}$, $\eta_{\rm RIFF}$, and Γ_d. The parameters $\alpha_{1,2}$ are found directly from the measurements of the response curve in Fig. 1(c); see Appendix B. The parameters $\eta_{\rm RIFF}$ and Γ_d can be chosen so as to describe the amplitude of the vibrations at the drive frequency as a function of the drive power shown in Fig. 2(c). The value of the drive power at the threshold of the instability $\mathcal{P}_{\rm th}$ is particularly sensitive to $\eta_{\rm RIFF}$. With these parameters, we describe the multitude of the observations, including not only the response but also the shape of the trajectories and its dependence on the drive power and frequency, Figs. 3(b) and 5(b), as well as the positions and intensities of the comb lines (see Appendix A 3).

In order to highlight the connection between the number of satellites in the frequency comb and the asymmetry of the trajectory of the limit cycle, Figs. 3(c) and 5(b) plot the amplitude of the Fourier components (red lines) on top of the amplitude of the measured comb lines (black dots). We find good agreement between the two.

V. SUMMARY AND OUTLOOK

We experimentally demonstrate that a resonantly driven single nanomechanical mode can display self-sustained vibrations in the rotating frame. No coupling to other modes is required. The self-sustained vibrations are strongly nonlinear, even though for the studied drive power the anharmonic part of the mode potential (in the laboratory frame) remains much smaller than the harmonic part. Because of the weak damping, the trajectories of the observed limit cycles in the rotating frame represent constant-quasienergy contours and thus provide a glimpse into the shape of the quasienergy surface. The Fourier components of the vibrations are manifested in the spectrum of the mode in the laboratory frame as extremely sharp equidistant peaks that form a frequency comb.

We find that the number of visible lines in the comb and the line spacing sensitively depend on the power and frequency of the close-to-resonance drive. This suggests a straightforward way of controlling the corresponding parameters, which is important for numerous applications of the phononic frequency combs. Other advantageous features of the system include the low power required to generate the comb and the very frequency range where multiple, equally spaced, spectral lines emerge simultaneously.

A good agreement of the theory with all experimental observations provides evidence of a qualitatively new mechanism of dissipation of driven vibrational systems, the resonantly induced friction force. Developing a microscopic theory of this force is a challenging problem that will be addressed in future work.

Data and analysis code are available at [52].

ACKNOWLEDGMENTS

We are grateful to S. W. Shaw for a useful discussion. J. S. O., D. K. J. B., W. B., and E. M. W. gratefully acknowledge financial support from the Deutsche Forschungsgemeinschaft (DFG, German Research Foundation) through Project-ID No. 425217212-SFB 1432. J. S. O. and E. M. W. further acknowledge funding from the European Union's Horizon 2020 Research and Innovation Programme under Grant Agreement No. 732894 (FET Proactive HOT), and the German Federal Ministry of Education and Research (Contract No. 13N14777) within the European QuantERA cofund project QuaSeRT. G. R. acknowledges funding and support from Provincia Autonoma di Trento and from CNR-INO. M. I. D. acknowledges support from the National Science Foundation, Grants No. DMR-1806473 and No. CMMI 1661618. M. I. D. is grateful for the warm hospitality at the University of Konstanz and at the Technical University of Munich.

APPENDIX A: THEORY

1. Hamiltonian dynamics of a resonantly driven mode

It is convenient to describe the Hamiltonian dynamics of a resonantly driven mode in two steps. The first step is the transition to the action-angle variables, I and θ, of the mode in the absence of driving. We relate these variables to the coordinate q and momentum p of the mode in the standard way [36] as

$$I = (2\pi)^{-1} \oint p dq, \qquad \theta = \frac{\partial}{\partial I} \int^{q} p dq,$$

with q and p being periodic in θ,

$$q(I, \theta + 2\pi) = q(I, \theta), \qquad p(I, \theta + 2\pi) = p(I, \theta).$$

An isolated mode performs periodic vibrations with $I =$ const. The phase linearly accumulates in time, $\dot{\theta} = \omega(I)$. The vibration frequency is $\omega(I) = dE/dI$, where E is the mode energy.

We note that the full Hamiltonian of the system includes the kinetic and potential energy of the isolated mode that we consider, but also a contribution from other degrees of freedom, such as other nanomechanical modes of the resonator, acoustic phonons, etc. The mode is coupled to these degrees of freedom. This leads to a renormalization of the parameters of the mode, in particular, of the dependence of its vibration frequency on I. The function $\omega(I)$ incorporates this renormalization along with the harmonic and anharmonic terms of the potential energy $U(q)$ of the isolated mode.

In the presence of a resonant drive, the Hamiltonian of the system takes the form

$$H = H_0 + H_F, \qquad H_0 = \int_0^I dI' \omega(I'),$$
$$H_F = -Fq(I, \theta) \cos \omega_d t, \tag{A1}$$

and the equations of motion read

$$\dot{I} = -\partial_\theta H_F, \qquad \dot{\theta} = \omega(I) + \partial_I H_F.$$

We consider the case where the driving is relatively weak, as explained in the main text. This means that the anharmonic part of the energy of the driven mode remains small compared to the harmonic part. In terms of I, the latter condition typically means that

$$I \ll I_{\text{anh}}, \qquad |\omega(I_{\text{anh}}) - \omega_0| \sim \omega_0 \equiv \omega(0). \tag{A2}$$

Here, I_{anh} is the value of the action variable where the change of the vibration frequency becomes comparable to ω_0.

The inequality (A2) is essentially the condition on the strength of the drive. We consider what we call a weak to a moderately strong drive or, equivalently, small to moderately large vibration amplitude. This implies that, for the characteristic values of I, the frequency change $F|\partial_I q|$ is small compared to ω_0 as is the rate of the change of the action $F|\partial_\theta q|$. However, the drive does not have to be small compared to the appropriately scaled frequency detuning $|\omega_d - \omega(I)| \ll \omega_0$. The interrelation between $F|\partial_I q|$ and $|\omega_d - \omega(I)|$ is arbitrary for typical values of I. For such a drive, the system remains far away from the region where the dynamics becomes chaotic.

The condition on the drive strength becomes more explicit if we expand $q(I, \theta)$ in I and $\omega_d - \omega_0$. The leading-order term in the expansion is

$$q(I, \theta) = (2I/M\omega_d)^{1/2} \cos \theta. \tag{A3}$$

Here, $(2I/M\omega_d)^{1/2}$ is the vibration amplitude for a given I. We note that nonlinear vibrations have overtones, which are disregarded in Eq. (A3). However, in the range of I we are interested in, the amplitudes of the overtones are small compared to the amplitude of the main tone.

To the order of magnitude, the vibration amplitude as a function of the drive amplitude can be estimated as $(2I_{\text{res}}/M\omega_d)^{1/2}$, where I_{res} is given by the standard condition of nonlinear resonance [25,45]

$$M\omega_d I_{\text{res}} [\omega_d - \omega(I_{\text{res}})]^2 \sim F^2.$$

The drive is weak to moderately strong, and the amplitude is small to moderately large provided

$$I_{\text{res}} \ll I_{\text{anh}}. \tag{A4}$$

Equation (A3) is the first term in the expansion of $q(I,\theta)$ in $I/I_{\rm anh} \ll 1$ and $|\omega_d - \omega(I)|/\omega_d \ll 1$. The smallness of the latter parameters justifies keeping the leading-order term in this expansion in the range given in Eq. (A4). We note that, in the same approximation, $p \approx -(2IM\omega_d)^{1/2}\sin\theta$.

a. Transition to slow variables

To analyze the resonant dynamics, we go to the rotating frame. This is done using the transformation

$$q = Q\cos\omega_d t + P\sin\omega_d t,$$
$$p = M\omega_d(-Q\sin\omega_d t + P\cos\omega_d t). \tag{A5}$$

In the approximation (A3), we have

$$Q^2 + P^2 = 2I/M\omega_d. \tag{A6}$$

We note that, in the approximation (A3),

$$Q = (2I/M\omega_d)^{1/2}\cos(\theta - \omega_d t),$$
$$P = -(2I/M\omega_d)^{1/2}\sin(\theta - \omega_d t),$$

which shows that Q and P are slow variables since $\dot\theta \approx \omega(I)$ and $\omega(I)$ is close to ω_d.

The transformation (A5) would be canonical if we used $Q/(M\omega_d)^{1/2}, P/(M\omega_d)^{1/2}$ instead of Q, P, but for comparison with the experiment below, it is more convenient to have Q and P of the same dimension as the coordinate q. As indicated in the main text, the variables Q and P correspond to the in-phase and quadrature components of the mode displacement. They slowly vary in time, remaining unchanged on the timescale $1/\omega_d$.

A time-dependent change of variables requires an appropriate change of the Hamiltonian [36]. In the present case, in the approximation (A6), the Hamiltonian becomes

$$H' \equiv H'(Q,P) = (H - \omega_d I)/M\omega_d.$$

In fact, we have changed from the variables I, θ, to the variables Q, P, with I related to Q, P by Eq. (A6).

The next step is averaging over the fast-oscillating terms in H'. First of all, we note that $I \propto Q^2 + P^2$ is a slow variable; fast-oscillating terms in $H_0 - \omega_d I$ are small. The major fast-oscillating terms in H' come from H_F. We evaluate them by substituting into H_F the expression (A5) for $q(I,\theta)$. Clearly, H_F has the term $-QF/2$ with no time-oscillating factors and two terms that contain the factors $\cos 2\omega_d t$ and $\sin 2\omega_d t$, respectively. Averaging over the time $2\pi/\omega_d$ allows us to eliminate these fast-oscillating terms. As a result, the time-averaged Hamiltonian $H'(Q,P)$ takes the form $g(Q,P)$ given in Eq. (3) of the main text, which we reproduce here for completeness:

$$g(Q,P) = (M\omega_d)^{-1}(H_0 - \omega_d I - QF/2),$$
$$I = M\omega_d(Q^2 + P^2)/2. \tag{A7}$$

In quantum terms, the eigenvalues of g give the Floquet eigenvalues of the driven mode [40–43].

b. Hamiltonian for a small effective Duffing parameter

In the above approximation, the response curve of a resonantly driven nonlinear oscillator is determined by the dependence of the frequency $\omega(I)$ on the action variable. In order to describe the observed response, it is sufficient to expand $\omega(I)$ to the second order in I,

$$\omega(I) = \omega_0 + \alpha_1 I + \alpha_2 I^2.$$

We then have, from Eqs. (A1) and (A7),

$$g(Q,P) = -\frac{1}{2}\delta\omega(Q^2+P^2) + \frac{M\omega_d}{8}\alpha_1(Q^2+P^2)^2 + \frac{(M\omega_d)^2}{24}\alpha_2(Q^2+P^2)^3 - \frac{F}{2M\omega_d}Q. \tag{A8}$$

Here,

$$\delta\omega = \omega_d - \omega_0 \tag{A9}$$

is the detuning of the drive frequency from the eigenfrequency of the mode.

The Hamiltonian dynamics of the mode in the rotating frame is described by the equations of motion,

$$\dot Q = \partial_P g(Q,P), \qquad \dot P = -\partial_Q g(Q,P). \tag{A10}$$

In the parameter range of interest, this dynamics consists of vibrations with a given g, with frequency $\nu(g)$ that depends on g.

As explained in the main text, the parameters $\alpha_{1,2}$ in Eq. (A8) depend on the nonlinearity of the potential of the mode $U(q)$ and also on the nonlinear coupling of the mode to other modes of the resonator, to the electron system [46], and to other degrees of freedom. Therefore, calculating them requires knowing multiple parameters and, in fact, the full characterization of the whole system, which is complicated if at all possible. This is essentially an unphysical task, as the parameters $\alpha_{1,2}$ are the only parameters that describe the resonant mode dynamics.

For completeness, we provide the expressions for $\alpha_{1,2}$ for an isolated mode with a nonlinear potential. In this potential, we have to keep the terms up to the sixth order in q to find $\alpha_{1,2}$,

$$U(q) = \frac{M}{2}\omega_0^2 q^2 + \frac{M}{3}\gamma_3 q^3 + \frac{M}{4}\gamma_4 q^4 + \frac{M}{5}\gamma_5 q^5 + \frac{M}{6}\gamma_6 q^6. \tag{A11}$$

The term proportional to q^4 is the nonlinear term kept in the Duffing model. In the main text, we used γ instead of γ_4 as the coefficient of this term. Obviously, the nonlinear part of the potential contains four parameters, whereas only two parameters, α_1 and α_2, are actually accessible to the experiment.

It is more convenient to calculate the frequency as a function of energy E,

$$\tilde{\omega}(E) \equiv \omega[I(E)] \approx \omega_0 + \alpha_1 \frac{E}{\omega_0} + \frac{E^2}{\omega_0^2}\left(\alpha_2 - \frac{\alpha_1^2}{2\omega_0}\right), \quad \text{(A12)}$$

and then find $\alpha_{1,2}$ from the expansion of $\tilde{\omega}(E)$ in a series in E. This expansion can be obtained from the expression

$$\tilde{\omega}(E) = \pi \Big/ \int_{q_{\min}(E)}^{q_{\max}(E)} \frac{dq}{\sqrt{2[E - U(q)]/M}}, \quad \text{(A13)}$$

where $q_{\max}(E)$ and $q_{\min}(E)$ $[q_{\max} > q_{\min}]$ are the turning points of the classical trajectory with a given E, i.e., $U(q_{\max}) = U(q_{\min}) = E$. Introducing

$$q_c = (q_{\max} + q_{\min})/2, \qquad L = (q_{\max} - q_{\min})/2,$$
$$q = q_c + K, \qquad K = L\sin\alpha,$$

we can write

$$E - U(q(K)) = (L^2 - K^2)\left[\mu_0 + \sum_{n=1}^{4} \mu_n K^n\right]. \quad \text{(A14)}$$

Here, the left-hand side is a polynomial of degree 6 in K with two real roots at $K = \pm L$ such that we can put the factor $(L^2 - K^2)$ up front, while the remaining part is a polynomial of degree 4 with the energy-dependent coefficients μ_i. This allows us to write

$$\int_{q_{\min}(E)}^{q_{\max}(E)} \frac{dq}{\sqrt{2[E-U(q)]/M}} = \frac{L}{\sqrt{2[E-U(q_c)]/M}} \int_0^{\pi} \frac{d\alpha}{\sqrt{1 + \sum_{n=1}^{4} \frac{L^2\mu_n}{E-U(q_c)} L^n \cos^n(\alpha)}}. \quad \text{(A15)}$$

Expanding $q_{\max}$ and $q_{\min}$ in powers of E, the square root can also be expanded in powers of E, and the integrals can be solved.

$$\alpha_1 = \frac{3}{4M\omega_0^2}\left(\gamma_4 - \frac{10\gamma_3^2}{9\omega_0^2}\right),$$
$$\alpha_2 = \frac{5\gamma_6}{4M^2\omega_0^3} - \frac{7\gamma_3\gamma_5}{2M^2\omega_0^5} - \frac{51\gamma_4^2}{64M^2\omega_0^5} + \frac{75\gamma_3^2\gamma_4}{16M^2\omega_0^7} - \frac{235\gamma_3^4}{144M^2\omega_0^9}. \quad \text{(A16)}$$

The parameter α_1 is proportional to the well-known expression for the Duffing parameter γ_4 renormalized due to the cubic nonlinearity of $U(q)$ [36]. It is this renormalization (along with other terms that contribute to the renormalization) that can make α_1 small, leading to the resonant response curve being significantly different from the conventional Duffing curve.

2. Dissipative dynamics

The dynamics of the mode in the rotating frame in the presence of dissipation is described by the equations [27]

$$\dot{Q} = \partial_P g + R_Q, \qquad \dot{P} = -\partial_Q g + R_P,$$
$$R_Q = -(\Gamma + F^2\Gamma_d)Q + \frac{\eta_{\mathrm{RIFF}}}{4M} FP^2,$$
$$R_P = -(\Gamma + F^2\Gamma_d)P - \frac{\eta_{\mathrm{RIFF}}}{4M} FQP. \quad \text{(A17)}$$

Here, we have taken into account the change of the friction coefficient Γ due to the driving-induced decay and described by Eq. (5) of the main text; the derivation is similar to that in Ref. [28]. The term proportional to η_{RIFF} describes the RIFF. We note that, for the microscopic mechanism of the RIFF considered in Ref. [27], the parameter η_{RIFF} is negative, and in what follows, we assume that $\eta_{\mathrm{RIFF}} < 0$.

The decay rates in Eq. (A17) should be compared with the frequency of oscillations $\nu(g)$ of the mode in the absence of decay. We assume that $\nu(g)$ is much larger than the decay rate. This is the case in the experiment, where the decay rate is extremely small. We note that $\nu(g) \ll \omega_0$; that is, the decay rate is small not only in the laboratory frame but also in the rotating frame.

For a small decay rate, the motion consists of oscillations with a given scaled quasienergy $g(Q,P) = g$, with g slowly evolving due to the decay. From Eq. (A17), this evolution is described by the equation

$$\dot{\bar{g}} = \overline{\partial_Q g R_Q + \partial_P g R_P} = \frac{\nu(g)}{2\pi} \int_{\mathcal{S}(g)} dQdP(\partial_Q R_Q + \partial_P R_P). \quad \text{(A18)}$$

Here, the overline implies averaging over the trajectory $g(Q,P) = g$, and $\mathcal{S}(g)$ is the area inside this trajectory. We note that the sign in the last line refers to the trajectory that corresponds to the large-amplitude branch of the response curve; for the low-amplitude branch, the sign is opposite.

a. Stable states and limit cycles

It follows from Eqs. (A17) and (A18) that, in the absence of the RIFF, we have $\dot{g} < 0$ on the large-amplitude branch. The stable state of the system $(Q_{\mathrm{st}}, P_{\mathrm{st}})$ is then the state with the minimal $g(Q,P)$, i.e., $g(Q_{\mathrm{st}}, P_{\mathrm{st}}) = g_{\min}$. It is given by the equation

$$[\partial_Q g(Q,0)]_{Q=Q_{\rm st}} = 0, \qquad P_{\rm st} = 0. \tag{A19}$$

It corresponds to the amplitude of forced vibrations $A = Q_{\rm st}$. In fact, the stable state is slightly shifted from the minimum of $g(Q,P)$ because of the dissipation. The shift is small where the dissipation rate is small compared to $\nu(g_{\rm min})$.

The solution of Eq. (A19) is used to find the parameters α_1 and α_2 from the dependence of A on both the frequency and the amplitude of the drive measured in the experiment, in a broad range of these parameters. We note that, in the regime of very small amplitudes where the linear decay rate has to be taken into account, the vibration amplitude A_0 is different from $Q_{\rm st}$. To the leading order in $\omega_0 - \omega_d$, the response is described by

$$\frac{F^2}{4M^2\omega_0^2} = A_0^2\left[\Gamma^2 + \left(-\delta\omega + M\alpha_1\frac{A_0^2\omega_0}{2} + M^2\alpha_2\frac{A_0^4\omega_0^2}{4}\right)^2\right]. \tag{A20}$$

For the values of A_0 where the term Γ^2 in Eq. (A20) can be disregarded, we have $A_0 = A = Q_{\rm st}$. For small damping, this happens already for a comparatively weak drive amplitude F.

For $A = Q_{\rm st}$, the decay rate λ near the stable state is

$$\lambda = \Gamma + F^2\Gamma_d + (\eta_{\rm RIFF}/8M)FQ_{\rm st}. \tag{A21}$$

This decay rate gives the half-width of the sideband peaks in the power spectrum of the driven mode, as seen in Ref. [39]. In the region where $F^2\Gamma_d$ can be disregarded, the rate λ decreases with the increasing drive amplitude F for $\eta_{\rm RIFF} < 0$ since $Q_{\rm st}$, as well as the factor F itself in the last term, increases with F. Overall, the decrease of λ with the increasing F is superlinear. This is in agreement with the decrease of the spectral linewidth in Fig. 2(b) of the main text.

The value of the drive parameters where $\lambda = 0$ corresponds to the Hopf bifurcation [47]. As the drive amplitude or frequency further increases, the state where $g = g_{\rm min}$ becomes unstable. The stable state is a limit cycle, which, for a small decay rate, is given by the equation $g(Q,P) = g$, with g given by the condition $\bar{\dot{g}} = 0$, or

$$\begin{aligned}\Gamma + F^2\Gamma_d &= -\frac{\eta_{\rm RIFF}F}{8M}\bar{Q}(g),\\ \bar{Q}(g) &= \frac{1}{\mathcal{S}(g)}\int_{\mathcal{S}(g)} Q\,dQ\,dP,\\ \mathcal{S}(g) &\equiv \int_{\mathcal{S}(g)} dQ\,dP.\end{aligned} \tag{A22}$$

In other words, the limit cycle is very close to the Hamiltonian trajectory in Eq. (A10). This trajectory depends on the drive parameters.

The mean coordinate in the rotating frame $\bar{Q}(g)$ decreases with the increasing g. Its value is maximal for $g = g_{\rm min}$. The system is unstable if the right-hand side of Eq. (A22) exceeds the left-hand side for $g = g_{\rm min}$. But as g increases, $\bar{Q}(g)$ falls off [27], and ultimately the condition (A22) is met.

The trajectories $g(Q,P) = \text{const}$ with the value of g given by Eq. (A22) are plotted in Figs. 3(b) and 5(a) of the main text. An important feature of these trajectories is that they are profoundly nonelliptical. Therefore, they have multiple Fourier components. It is this feature that leads to the onset of the frequency comb in the laboratory frame.

3. Frequency comb in the power spectrum

We now discuss the power spectrum of the mode where, in the rotating frame, it vibrates with a given value of $g(Q,P) = g$, i.e., with a given quasienergy. The spectral density of fluctuations of the displacement $q(t)$ of the resonantly driven mode near the driving frequency ω_d has the form

$$\begin{aligned}S(\omega) &= \frac{1}{2t_l}\left|\int_{-t_l}^{t_l} dt\, q(t)e^{i\omega t}\right|^2\\ &\approx \frac{1}{8t_l}\left|\int_{-t_l}^{t_l} dt[Q(t)+iP(t)]e^{i(\omega-\omega_d)t}\right|^2,\end{aligned} \tag{A23}$$

where it is implied that $t_l \to \infty$. We have assumed that $|\omega - \omega_d| \ll \omega_d$ and expressed $q(t)$ in terms of the slowly varying-in-time quadratures $Q(t)$ and $P(t)$ using Eq. (A5).

Using the Hamiltonian equations of motion (A10) for $Q(t)$ and $P(t)$, we can write

$$[Q(t)+iP(t)]_g = \sum_m z_m(g)e^{im\nu(g)t}. \tag{A24}$$

Here, $[\cdot]_g$ indicates that the value is evaluated for a given $g(Q,P)$, and $\nu(g)$ is the oscillation frequency in the rotating frame. The Fourier components z_m are also determined by the value of g. For a resonantly driven Duffing oscillator, $\alpha_2 = 0$, they were calculated and used earlier [48–50], taking into account that, in this case, the trajectories in Eq. (A10) are expressed in terms of the Jacobi elliptic functions. The parameters z_m are also given in Ref. [27]; however, the expressions of the latter paper for $m < 0$ need to be corrected to account for the proper parallelogram of periods of the relevant functions.

From Eqs. (A23) and (A24), the power spectrum $S(\omega) = S_g(\omega)$ of the driven oscillator for a given $g(Q,P)$ is

$$S_g(\omega) = \frac{\pi}{2}\sum_m |z_m(g)|^2\delta[\omega - \omega_d + m\nu(g)]. \tag{A25}$$

The spectrum (A25) is a frequency comb. It consists of a set of equidistant peaks separated by $\nu(g)$. The intensity (area)

of the peaks is given by the Fourier components $z_m(g)$; note that, generally, $z_{-m}(g) \neq z_m^*(g)$.

For $\alpha_2 \neq 0$, the Fourier components $z_m(g)$ are found from the numerical solution of Eq. (A10). The results for $|z_m(g)|$ are presented in Figs. 3(c) and 5(b) of the main text.

We note that, below the threshold of instability, the mode performs fluctuation-induced vibrations about Q_{st} and P_{st}. They lead to peaks in the power spectrum at frequencies $\omega_d \pm \nu(g_{\mathrm{min}})$. Slightly above the threshold, the stable value of g as given by Eq. (A22) is close to g_{min}. The vibrations in the rotating frame are nearly sinusoidal in this range, and their frequency is close to $\nu(g_{\mathrm{min}})$. Therefore, the major spectral manifestation of going through the threshold is the narrowing of the spectral lines, as indeed seen in the experiment.

APPENDIX B: CALIBRATION

In the experiment, the drive amplitude F is not directly accessible. Instead, the rf input voltage V_{in} that determines the amplitude of the ac voltage is controlled. The mode vibrations are measured by resonantly driving a microwave cavity that contains the nanobeam. The nanobeam vibration induces sidebands in the microwave signal. The signal is demodulated and mixed with the rf signal to find the in-phase Q and quadrature P components of the vibrations in volts. The vibration amplitude in volts is $V_{\mathrm{out}} = \sqrt{Q^2 + P^2}$. We assume that both voltage signals, V_{in} and V_{out}, relate to the physical quantities in a linear way since they are small compared to the applied dc voltage. We write

$$A = aV_{\mathrm{out}}, \qquad F/M = bV_{\mathrm{in}},$$

with a and b being calibration constants. The constant a is of the order of 2.5×10^{-5} m/V; see Ref. [39].

For weak drives, the force-dependent friction terms, Eqs. (4) and (5) in the main text, can be neglected, and the response of the system is described by Eq. (A20). Expressing F and A in terms of V_{in} and V_{out} in this equation, we find that the needed model parameters are the conversion factor

$$c = b^2/4\omega_0^2\Gamma^2a^2,$$

the linewidth $2\Gamma/2\pi$, the frequency ω_0, and the nonlinearity parameters $M\alpha_1a^2$ and $M^2\alpha_2a^4$.

The parameters can be determined from fits in a systematic way, making use of the fact that, for small drive powers and therefore small amplitudes, the contribution from the term with α_2—and, for very small drive powers, also the contribution from α_1—can be neglected. Assuming a constant noise floor of 1.5×10^{-6} mV, we fit the different regimes. We start at a drive power of -56 dBm with the Lorentzian response; proceed to a drive power of -37 dBm with the Duffing fit, where we take the contribution from α_1 into account; and finally fit the response at -24 dBm with the full Eq. (A20) to determine α_2.

Except for the plots in Figs. 3(b) and 5(a) of the main text, all data and theoretical calculations belong to the same set of calibration parameters. For the data of the trajectory measurements, namely, the data shown in Figs. 3(b) and 5(a), the conversion factor a is different. Using a second set of response measurements in the different regimes, we reconstruct the ratio between the two a factors by comparing the fit values for α_1 between the two sets of response measurements. We use their ratio r to scale the data of Figs. 3(b) and 5(a).

The phenomenological parameters of the dissipation mechanisms are fixed in a separate step. Seeking the best description of the amplitude of the vibrations at the drive frequency as a function of the drive power shown in Fig. 2(c), we set Γ_d to some value and fix η_{RIFF} by demanding that the Hopf bifurcation occurs at the threshold power $\mathcal{P}_{\mathrm{th}}$, meaning that the parameter λ given by Eq. (A21) goes to zero at $\mathcal{P}_{\mathrm{th}}$.

The values we find are

$$c = 5.28 \times 10^{-3}, \qquad \omega_0 = 4.10 \times 10^7/\mathrm{s},$$
$$r = 1.21, \qquad Ma^2\alpha_1 = 45.2/\mathrm{V}^2,$$
$$M^2a^4\alpha_2 = 0.400\ \mathrm{s/V}^4, \qquad a^2\eta_{\mathrm{RIFF}} = -2.81 \times 10^{-3}\ \mathrm{s/V}^2,$$
$$2\Gamma/2\pi = 21.1/\mathrm{s}, \qquad M^2a^2\Gamma_d = 4.5 \times 10^{-16}\ \mathrm{s}^3/\mathrm{V}^2.$$

APPENDIX C: ADDITIONAL EXPERIMENTAL OBSERVATIONS

1. Mechanical eigenmodes

Several measurements have been performed to verify that only one mechanical mode, the fundamental OOP mode of the 55-μm-long nanostring under investigation ($f_0 = 6.529$ MHz) is involved in the frequency comb formation.

Generally, a dc voltage applied to the dielectric control electrodes tunes the eigenfrequencies and can induce an appreciable coupling between the out-of-plane and in-plane modes of the nanostring [33,51]. However, as already discussed in the main text, all measurements in this work have been done at a constant dc voltage of 5 V where all modes are tuned sufficiently far from resonance so that the coupling is effectively weak and the out-of-plane and in-plane modes can be considered as independent eigenmodes of the system.

Besides higher harmonic eigenmodes, also the modes of additional nanostrings on the sample need to be considered to obtain a complete picture. The sample hosts a series of 12 nanostring resonators with lengths ranging from 33 μm to 55 μm, which are shunted between the same pair of control electrodes. Out of the twelve resonators, six are

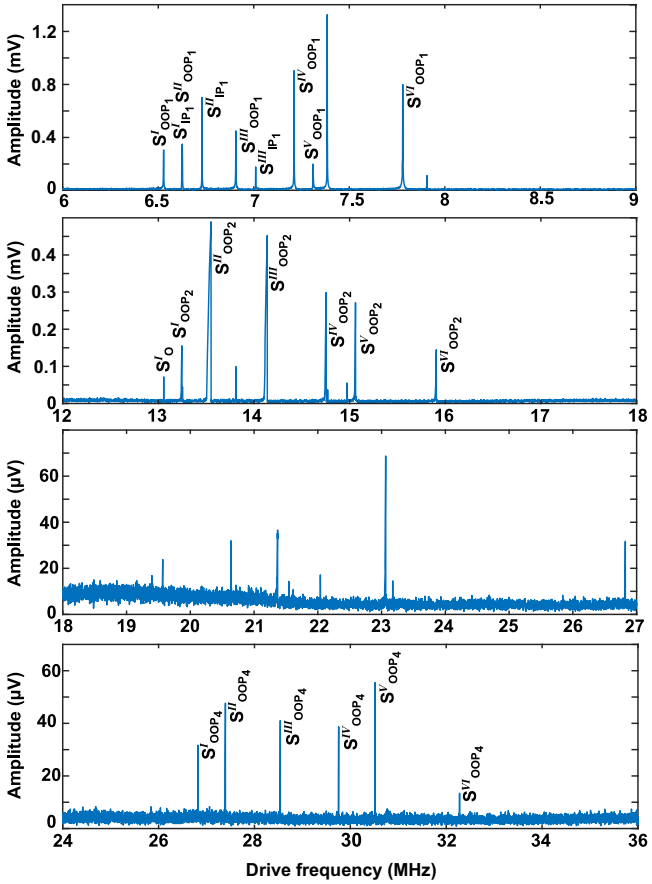

FIG. 6. Mode spectra of the investigated sample hosting six working nanostring resonators. The applied drive powers are −20 dBm, −10 dBm, and −4 dBm, from top to bottom; the lowest two panels are both measured for a drive power of −4 dBm. The lowest-frequency mode at approximately 6.5 MHz is the OOP mode of the longest string discussed in this work. Identified modes are labeled by the string number (S^{I} to S^{VI}, from the longest to the shortest working nanostring), the mode polarization (OOP or IP for out-of-plane and in-plane modes), and the harmonic (1 to 4 from the fundamental up to the fourth harmonic). The label S^{I}_{O} refers to the second overtone at exactly twice the eigenfrequency of the OOP mode at 6.5 MHz. It does not correspond to an eigenmode of the system. The spurious mode at 19.56 MHz in the third panel remains unlabeled. Other modes in this panel are third harmonics, which, however, could not be unambiguously assigned to the eigenmodes of the six-string system.

working, including the longest one, which is the nanostring we are focusing on in this work. As it is the longest nanostring on the sample, its OOP mode is the lowest-frequency eigenmode found. Note that the fundamental in-plane eigenmode occurs at a slightly higher eigenfrequency as a result of the nanostring's width slightly exceeding its thickness. The full mode spectrum of the sample is shown in Fig. 6. The drive frequency was swept up to a frequency of 36 MHz while recording the response of the forced vibrations at the drive frequency. The measurement clearly demonstrates that while there are many mechanical

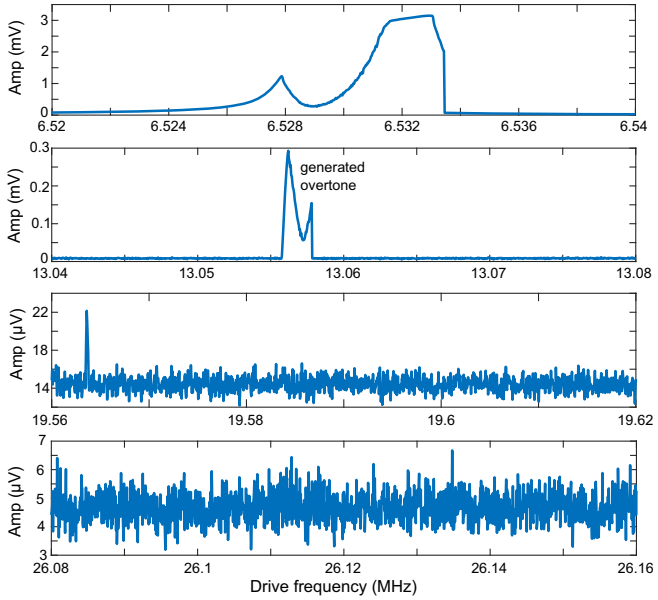

FIG. 7. Frequency response measurement in the RIFF regime (drive power 0 dBm), sweeping the drive frequency through the eigenfrequency of the OOP mode. The four lines show the response of the sample at the drive frequency, as well as at 2, 3, and 4 times its value.

modes on the sample, there is no $1:n$ internal resonance between the OOP mode under investigation and any of the other modes.

Figure 7 shows a frequency response measurement where we sweep the drive frequency around the eigenfrequency of the OOP mode under investigation in the regime of self-sustained vibrations in the rotating frame, along with the response of the system at 2, 3, and 4 times the drive frequency. The only signatures found at higher frequencies are the second overtone at exactly twice the drive frequency. We could not resolve the third and fourth overtones, presumably because of their small amplitudes for the drive power used. The peak at approximately 19.56 MHz is seen with and without drive and is most likely a feature of the instrument. This observation confirms and extends the conclusion drawn from Fig. 1(d) of the main text that no additional modes are nonlinearly excited, even when driving slightly off resonance.

[1] S. T. Cundiff, J. Ye, and J. L. Hall, *Optical Frequency Synthesis Based on Mode-Locked Lasers*, Rev. Sci. Instrum. **72**, 3749 (2001).
[2] T. Udem, R. Holzwarth, and T. W. Hänsch, *Optical Frequency Metrology*, Nature (London) **416**, 233 (2002).
[3] T. Fortier and E. Baumann, *20 Years of Developments in Optical Frequency Comb Technology and Applications*, Commun. Phys. **2**, 153 (2019).
[4] N. Picqué and T. W. Hänsch, *Frequency Comb Spectroscopy*, Nat. Photonics **13**, 146 (2019).

[5] L. Chang, S. Liu, and J. E. Bowers, *Integrated Optical Frequency Comb Technologies*, Nat. Photonics **16**, 95 (2022).

[6] P. Del'Haye, A. Schliesser, O. Arcizet, T. Wilken, R. Holzwarth, and T. J. Kippenberg, *Optical Frequency Comb Generation from a Monolithic Microresonator*, Nature (London) **450**, 1214 (2007).

[7] T. J. Kippenberg, R. Holzwarth, and S. A. Diddams, *Microresonator-Based Optical Frequency Combs*, Science **332**, 555 (2011).

[8] R. P. Erickson, M. R. Vissers, M. Sandberg, S. R. Jefferts, and D. P. Pappas, *Frequency Comb Generation in Superconducting Resonators*, Phys. Rev. Lett. **113**, 187002 (2014).

[9] A. Erbe, H. Krömmer, A. Kraus, R. H. Blick, G. Corso, and K. Richter, *Mechanical Mixing in Nonlinear Nanomechanical Resonators*, Appl. Phys. Lett. **77**, 3102 (2000).

[10] R. B. Karabalin, M. C. Cross, and M. L. Roukes, *Nonlinear Dynamics and Chaos in Two Coupled Nanomechanical Resonators*, Phys. Rev. B **79**, 165309 (2009).

[11] A. A. Savchenkov, A. B. Matsko, V. S. Ilchenko, D. Seidel, and L. Maleki, *Surface Acoustic Wave Opto-mechanical Oscillator and Frequency Comb Generator*, Opt. Lett. **36**, 3338 (2011).

[12] L. S. Cao, D. X. Qi, R. W. Peng, M. Wang, and P. Schmelcher, *Phononic Frequency Combs through Nonlinear Resonances*, Phys. Rev. Lett. **112**, 075505 (2014).

[13] A. Ganesan, C. Do, and A. Seshia, *Phononic Frequency Comb via Intrinsic Three-Wave Mixing*, Phys. Rev. Lett. **118**, 033903 (2017).

[14] M. J. Seitner, M. Abdi, A. Ridolfo, M. J. Hartmann, and E. M. Weig, *Parametric Oscillation, Frequency Mixing, and Injection Locking of Strongly Coupled Nanomechanical Resonator Modes*, Phys. Rev. Lett. **118**, 254301 (2017).

[15] D. A. Czaplewski, C. Chen, D. Lopez, O. Shoshani, A. M. Eriksson, S. Strachan, and S. W. Shaw, *Bifurcation Generated Mechanical Frequency Comb*, Phys. Rev. Lett. **121**, 244302 (2018).

[16] R. Wei, J. Lee, T. Mei, Y. Xie, M. S. Islam, S. Mandal, and P. X.-L. Feng, *A Self-Sustained Frequency Comb Oscillator via Tapping Mode Comb-Drive Resonator Integrated with a Feedback ASIC*, in *Proceedings of 2019 IEEE 32nd International Conference on Micro Electro Mechanical Systems (MEMS)* (2019), pp. 165–168.

[17] S. Houri, D. Hatanaka, Y. M. Blanter, and H. Yamaguchi, *Modal Analysis Investigation of Mechanical Kerr Frequency Combs*, in *Topics in Nonlinear Mechanics and Physics*, Springer Proceedings in Physics, edited by M. Belhaq (Springer, Singapore, 2019), pp. 141–157.

[18] M. Park and A. Ansari, *Formation, Evolution, and Tuning of Frequency Combs in Microelectromechanical Resonators*, J. Microelectromech. Syst. **28**, 429 (2019).

[19] Z. Qi, C. R. Menyuk, J. J. Gorman, and A. Ganesan, *Existence Conditions for Phononic Frequency Combs*, Appl. Phys. Lett. **117**, 183503 (2020).

[20] A. Chiout, F. Correia, M.-Q. Zhao, A. T. C. Johnson, D. Pierucci, F. Oehler, A. Ouerghi, and J. Chaste, *Multi-Order Phononic Frequency Comb Generation within a* MoS_2 *Electromechanical Resonator*, Appl. Phys. Lett. **119**, 173102 (2021).

[21] S. Houri, M. Asano, H. Okamoto, and H. Yamaguchi, *Self-Sustained Libration Regime in Nonlinear Microelectromechanical Devices*, Phys. Rev. Appl. **16**, 064015 (2021).

[22] A. Keşkekler, H. Arjmandi, P. G. Steeneken, and F. Alijani, *Symmetry-Breaking-Induced Frequency Combs in Graphene Resonators*, Nano Lett. **22**, 6048 (2022).

[23] S. Khan and H. E. Türeci, *Frequency Combs in a Lumped-Element Josephson-Junction Circuit*, Phys. Rev. Lett. **120**, 153601 (2018).

[24] Y. Lu, I. Strandberg, F. Quijandría, G. Johansson, S. Gasparinetti, and P. Delsing, *Propagating Wigner-Negative States Generated from the Steady-State Emission of a Superconducting Qubit*, Phys. Rev. Lett. **126**, 253602 (2021).

[25] V. I. Arnold, *Mathematical Methods of Classical Mechanics*, 2nd ed. (Springer, New York, 1989).

[26] E. Fermi, *The Raman Effect of Carbon Dioxide*, Z. Phys. **71**, 250 (1931).

[27] M. I. Dykman, G. Rastelli, M. L. Roukes, and E. M. Weig, *Resonantly Induced Friction and Frequency Combs in Driven Nanomechanical Systems*, Phys. Rev. Lett. **122**, 254301 (2019).

[28] M. I. Dykman, *Heating and Cooling of Local and Quasi-local Vibrations by Non-Resonance Field*, Sov. Phys. Solid State **20**, 1306 (1978), https://web.pa.msu.edu/people/dykman/pub06/Sov.Phys.Sol.St._78.pdf.

[29] M. Aspelmeyer, T. J. Kippenberg, and F. Marquardt, *Cavity Optomechanics*, Rev. Mod. Phys. **86**, 1391 (2014).

[30] Preliminary experimental data on the onset of a frequency comb in a nanomechanical resonator were presented in the master thesis by Johannes Kölbl and were shown by E. M. Weig at the conference on Frontiers of Nanomechanical Systems 2019,https://fns2019.caltech.edu.

[31] N. E. Bousse, J. M. L. Miller, A. L. Alter, C. P. Cameron, H.-K. Kwon, G. D. Vukasin, and T. W. Kenny, *Negative Nonlinear Dissipation in Microelectromechanical Beams*, J. Microelectromech. Syst. **29**, 954 (2020).

[32] T. Faust, P. Krenn, S. Manus, J. P. Kotthaus, and E. M. Weig, *Microwave Cavity-Enhanced Transduction for Plug and Play Nanomechanics at Room Temperature*, Nat. Commun. **3**, 728 (2012).

[33] J. Rieger, T. Faust, M. J. Seitner, J. O. P. Kotthaus, and E. M. Weig, *Frequency and Q Factor Control of Nanomechanical Resonators*, Appl. Phys. Lett. **101**, 103110 (2012).

[34] Q. P. Unterreithmeier, E. M. Weig, and J. P. Kotthaus, *Universal Transduction Scheme for Nanomechanical Systems Based on Dielectric Forces*, Nature (London) **458**, 1001 (2009).

[35] A. Bachtold, J. Moser, and M. I. Dykman, *Mesoscopic Physics of Nanomechanical Systems*, arXiv:2202.01819 [Rev. Mod. Phys. (to be published)].

[36] L. D. Landau and E. M. Lifshitz, *Mechanics*, 3rd ed. (Elsevier, Amsterdam, 2004).

[37] J. S. Ochs, G. Rastelli, M. Seitner, M. I. Dykman, and E. M. Weig, *Resonant Nonlinear Response of a Nanomechanical System with Broken Symmetry*, Phys. Rev. B **104**, 155434 (2021).

[38] S. M. Soskin, R. Mannella, and P. V. E. McClintock, *Zero-Dispersion Phenomena in Oscillatory Systems*, Phys. Rep. **373**, 247 (2003).

[39] J. S. Huber, G. Rastelli, M. J. Seitner, J. Kölbl, W. Belzig, M. I. Dykman, and E. M. Weig, *Spectral Evidence of Squeezing of a Weakly Damped Driven Nanomechanical Mode*, Phys. Rev. X **10**, 021066 (2020).

[40] J. H. Shirley, *Solution of the Schrödinger Equation with a Hamiltonian Periodic in Time*, Phys. Rev. **138**, B979 (1965).

[41] Y. B. Zel'dovich, *The Quasienergy of a Quantum-Mechanical System Subjected to a Periodic Action*, Sov. Phys. JETP **24**, 1006 (1967), http://www.jetp.ras.ru/cgi-bin/dn/e_024_05_1006.pdf.

[42] V. I. Ritus, *Shift and Splitting of Atomic Energy Levels by the Field of an Electromagnetic Wave*, Sov. Phys. JETP **24**, 1041 (1967), http://www.jetp.ras.ru/cgi-bin/dn/e_024_05_1041.pdf.

[43] H. Sambe, *Steady States and Quasienergies of a Quantum-Mechanical System in an Oscillating Field*, Phys. Rev. A **7**, 2203 (1973).

[44] B. van der Pol, *On Relaxation-Oscillations*, London Edinburgh Dublin Philos. Mag. J. Sci. **2**, 978 (2009).

[45] E. Ott, *Chaos in Dynamical Systems* (Cambridge University Press, Cambridge, England, 2002).

[46] K. Moskovtsev and M. I. Dykman, *Strong Vibration Nonlinearity in Semiconductor-Based Nanomechanical Systems*, Phys. Rev. B **95**, 085426 (2017).

[47] J. Guckenheimer and P. Holmes, *Nonlinear Oscillators, Dynamical Systems and Bifurcations of Vector Fields* (Springer-Verlag, New York, 1997).

[48] M. I. Dykman and V. N. Smelyanskii, *Quantum-Theory of Transitions between Stable States of a Nonlinear Oscillator Interacting with the Medium in a Resonant Field*, Zh. Eksp. Teor. Fiz. **94**, 61 (1988) [Sov. Phys. JETP **67**, 1769 (1988)], http://www.jetp.ras.ru/cgi-bin/dn/e_067_09_1769.pdf.

[49] M. I. Dykman and M. V. Fistul, *Multiphoton Antiresonance*, Phys. Rev. B **71**, 140508(R) (2005).

[50] L. Guo, V. Peano, M. Marthaler, and M. I. Dykman, *Quantum Critical Temperature of a Modulated Oscillator*, Phys. Rev. A **87**, 062117 (2013).

[51] T. Faust, J. Rieger, M. J. Seitner, P. Krenn, J. P. Kotthaus, and E. M. Weig, *Nonadiabatic Dynamics of Two Strongly Coupled Nanomechanical Resonator Modes*, Phys. Rev. Lett. **109**, 037205 (2012).

[52] Data and analysis code are available at 10.5281/zenodo.7322874.